Science Bulletin 64 (2019) 1095–1102

Contents lists available at ScienceDirect

Science Bulletin

journal homepage: www.elsevier.com/locate/scib

Science Bulletin
www.scibull.com

Article

Controlled synthesis of single cobalt atom catalysts via a facile one-pot pyrolysis for efficient oxygen reduction and hydrogen evolution reactions

Yao Wang [a,b,1], Linhui Chen [a,1], Zhanxin Mao [a], Lishan Peng [a], Rui Xiang [a], Xianyi Tang [a], Jianghai Deng [a], Zidong Wei [a,*], Qiang Liao [c]

[a] Chongqing Key Laboratory of Chemical Process for Clean Energy and Resource Utilization, College of Chemistry and Chemical Engineering. Chongqing University, Chongqing 400044, China
[b] Institute of New-Energy and Low-Carbon Technology, Sichuan University, Chengdu 610065, China
[c] Key Laboratory of Low-Grade Energy Utilization Technologies and Systems, Chongqing University, Chongqing 400044, China

ARTICLE INFO

Article history:
Received 16 April 2019
Received in revised form 31 May 2019
Accepted 6 June 2019
Available online 10 June 2019

Keywords:
Carbon nanocomposites
Single-atom catalysts
H_2 evolution
O_2 reduction
Zn-O_2 battery

ABSTRACT

Metal-nitrogen doped carbon catalysts (M-N/C) with abundantly accessible M-N_x sites, particularly single metal atom M-N/C (SAM-N/C), have been developed as a substitute for expensive Pt-based catalysts. These catalysts are used to increase the efficiency of otherwise sluggish oxygen reduction reactions (ORR) and hydrogen evolution reactions (HER). However, although the agglomerated metal nanoparticles are usually easy to form, they are very difficult to remove due to the protective surface-coating carbon layers, a factor that significantly hampers SAM-N/C fabrication. Herein, we report a one-step pyrolysis approach to successfully fabricate single cobalt atom Co-N/C (SACo-N/C) by using a Co^{2+}-SCN^- coordination compound as the metal precursor. Thanks to the decomposition of Co^{2+}-SCN^- compound at lower temperature than that of carbon layer deposition, Co-rich particles grow up to larger ones before carbon layers formation. Even though encapsulated by the carbon layers, it is difficult for the large Co-rich particle to be completely sealed. And thus, it makes the Co atoms possible to escape from incomplete carbon layer, to coordinate with nitrogen atoms, and to form SACo-N/C catalysts. This SACo-N/C exhibits excellent performances for both ORR (half-wave potential of 0.878 V) and HER (overpotential at 10 mA/cm^2 of 178 mV), and is thus a potential replacement for Pt-based catalysts. When SACo-N/C is integrated into a Zn-O_2 battery, battery with high open-circuit voltage (1.536 V) has high peak power density (266 mW/cm^2) and large gravimetric energy density (755 mA h/g_{Zn}) at current densities of 100 mA/cm^2. Thus, we believe that this strategy may offer a new direction for the effective generation of SAM-N/C catalysts.

1. Introduction

The current energy crisis and environmental problems has encouraged the development of novel electrochemical energy conversion and storage devices, such as water splitting devices, fuel cells and metal-air batteries [1–7]. Nevertheless, these devices still suffer from limited efficiency, dominantly as a result of the sluggish kinetics of electrochemical reactions. Oxygen reduction reactions (ORR) and hydrogen evolution reactions (HER), occurring at the cathode of the above devices, play the determinant role in the overall energy efficiency but require a large amount of Pt-based catalysts to achieve high efficiency [8–12]. Pt-based catalysts, while effective, have high associated costs, and rely on scarce and vulnerable resources, and it is therefore crucial to develop cost-effective materials with high activity and long-term durability [5,13–16].

Metal-nitrogen doped carbon catalysts (M-N/C, M = Fe, Co, Ni, etc.) have been proposed as the most promising alternatives to Pt-based catalysts for ORR and HER, of which M-N_x sties have been regarded as the most active centers [17–21]. Generally, a structure with abundantly accessible M-N_x sites is desirable for high-performance M-N/C catalysts but conventional M-N/C catalysts contain inhomogeneous components such as agglomerated metal nanoparticles coated by carbon shell, leading to the inevitable loss of porosity and an accordingly low density of active M-N_x sites [22–28]. Recently, single atom catalysts with both high maximum

* Corresponding author.
E-mail address: zdwei@cqu.edu.cn (Z. Wei).
[1] Yao Wang and Linhui Chen contributed equally to this work.

https://doi.org/10.1016/j.scib.2019.06.012
2095-9273/

metal atom utilization efficiencies and dispersion densities of active M-N_x sites have emerged [29,30]. Taking advantage of the strong coordination between ligands and transition metal atoms in porous metal-organic frameworks (MOFs), a series of M-N/C electrocatalysts with M-N_x active sites (SAM-N/C) distributed at the atomic level have been successfully fabricated via using MOFs directly as the precursors or hosts [31–35]. Other template-assistant-pyrolysis methods have also been proposed to construct SAM-N/C catalysts using the confinement effect [36–40]. Nonetheless, all of these methods can suffer from high costs, as is the case for MOF or metalloporphyrin complexes, and complex post-treatment issues that significantly hamper their practical applications. Thus, the fabrication of SAM-N/C catalysts using a straightforward and cost-efficient synthetic method remains an important research direction.

Herein, we report the synthesis of a single atom Co-N/C catalyst (SACo-N/C) for ORR and HER via a one-pot solid-state reaction method using a Co^{2+}-SCN^- coordination compound (Co^{2+}-SCN^-) as the metal precursor. Inexpensive urea and glucose were chosen as the nitrogen and carbon precursors, respectively. Owing to the decomposition of the Co^{2+}-SCN^- precursor, the temperature of formation of the Co-rich particles is shown to be lower than the temperature of carbon deposition. This separated formation process of Co-rich particles and graphitic carbon results in the formation of large Co-rich agglomerates, and thereby hampers the formation of small Co-rich particles well-encapsulated by carbon layer (Co@C), which would form as if Co-rich particles and graphitic carbon were produced at the same temperature/time. Because Co-rich particles have grown up large, it is difficult to be completely and tightly encapsulated by carbon layers. In this case, there is possibility for cobalt atoms in large Co-rich particles to escape from the discontinuous carbon layers, move to dangled nitrogen atoms, and coordinate with each other. In contrast, the conventional method generally leads to form metal-rich particles@carbon shell structure through high-temperature pyrolysis processes. Non-coordinated Co atoms and impurities can be easily removed by acid treatment, left SACo-N/C only. To the best of our knowledge, this is the first report of the preparation of SAM-N/C catalysts using inexpensive small molecules for use in ORR and HER. Unlike SAM-N/C catalysts obtained using MOFs as the precursor, these as-prepared SACo-N/C exhibit a two-dimensional graphene structure, which may impart enhanced accessibility of the active sites. An increased electron transfer ability may be also ensured for SACo-N/C owing to its well-defined graphene structure. SACo-N/C catalysts thus exhibit excellent performances in both ORR and HER.

2. Materials and methods

2.1. Synthesis of catalysts

2.1.1. Preparation of SACo-N/C precursor

Urea, glucose, $CoCl_2{\cdot}6H_2O$ and NaSCN were mixed in a 50 mL beaker with ethanol (30 mL). After ultrasonic stirring for 5 min, the homogeneous solution was transferred into an oven at 60 °C for 8 h until the ethanol was completely evaporated. Then, the recrystallized solid was ball-milled at 700 r/min for 0.5 h to obtain the catalyst precursor.

2.1.2. Synthesis of SACo-N/C, SACo-N/C-900, SA-Co-N/C-1000

The obtained precursor was introduced into a tube furnace and pyrolyzed under a N_2 atmosphere at 800, 900, and 1,000 °C for 60 min with a heating rate of 10 °C/min. After cooling to room temperature under nitrogen atmosphere, the catalysts SACo-N/C-pre, SACo-N/C-900-pre and SA-Co-N/C-1000-pre were acquired. These as-prepared catalysts were soaked in 0.5 mol/L H_2SO_4 at 80 °C for 8 h. Finally, after washing with distilled water and vacuum drying, SACo-N/C, SACo-N/C-900 and SA-Co-N/C-1000 were obtained. The mass ratio of urea to glucose was 60:1 and that of organics (total mass of urea and glucose) and metal salt ($CoCl_2{\cdot}6H_2O$) was 240:1. The molar ratio of SCN^- and Co^{2+} was maintained at 2:1.

2.1.3. Synthesis of Co-N/C

Co-N/C was prepared using the procedure described for SACo-N/C-800 without NaSCN addition.

2.1.4. Synthesis of N/C

N/C was prepared using the procedure described for SACo-N/C-800 without $CoCl_2{\cdot}6H_2O$ addition.

2.1.5. Synthesis of the catalysts at different temperature for XRD test

Catalysts collected at different temperatures were prepared by pyrolysis of the SACo-N/C and Co-N/C precursors. The pyrolysis directly elevates temperature to the specific temperature and subsequently cools down, i.e., there is no thermostatic process.

2.2. Characterization of catalysts

The morphology of catalysts was observed using field emission scanning electron microscopy (FE-SEM, JSM-7800F, JEOL), transmission electron microscopy (TEM, Zeiss LIBRA 200) operated at 200 kV and TEM (JEOL JEM-2100) operated at 200 kV. High-angle annular dark-field scanning TEM (HAADF-STEM) used a Titan 80-300 STEM operating at 300 kV, equipped with a spherical probe aberration corrector. Crystal structures were confirmed using automated X-ray diffraction equipment (XRD, RigakuD/MaXIIIA). X-ray photoelectron spectroscopy (XPS) was conducted using a Kratos XSAM800 spectrometer equipped with a monochromatic Al X-ray source (Al KR, 1.4866 keV), and the binding energy was calibrated using 284.6 eV as the C 1s peak energy. Thermogravimetric analysis/differential thermal analysis (TGA/DTA) was carried out using a NETZSCH TGASTA 409 PC analyzer with a heating rate of 10 °C/min. Raman spectra were acquired using a micro-Raman spectrometer (RFS-100/S) with an incident laser wavelength of 523.5 nm.

All electrochemical measurements were performed using a standard three-electrode cell at room temperature on a Parstat 2273 potentiostat/galvanostat workstation and a model 636 rotational system (AMETEK) at room temperature. The cell comprises a glassy carbon working electrode (GC electrode, 5 mm in diameter, PINE:AFE3T050GC), an Ag/AgCl (saturated KCl) reference electrode, and a graphite rod counter electrode. The working electrodes were prepared by applying catalyst ink onto glassy carbon (GC) disk electrodes. Rotating ring disk electrode (RRDE) measurements were conducted using a ring disk electrode with a GC disk tip (4 mm in diameter) and a Pt ring (inner diameter 5 mm, outer diameter 7 mm).

For alkaline media, the activity of the samples was characterized at room temperature in 1 mol/L aqueous KOH (HER) and 0.1 mol/L aqueous KOH (ORR), respectively. Cyclic voltammetry (CV) tests for catalysts were performed at room temperature with a scan rate of 50 mV/s in the potential range 0–1.2 V (vs. RHE). Linear sweep voltammetry (LSV) was obtained either in the potential range −0.6 to 0.1 V (vs. RHE) for HER, and in an O_2-saturated 0.1 mol/L KOH in the potential range 0–1.1 V (vs. RHE) for ORR, both at a scan rate of 10 mV/s. For acid media, the activity of the samples was characterized at room temperature in 0.5 mol/L aqueous H_2SO_4 for HER and 0.1 mol/L aqueous $HClO_4$ for ORR. The CV tests for catalysts were performed at room temperature at a scan rate of 50 mV/s in the potential range 0–1.2 V (vs. RHE). LSV was obtained in the potential range −0.6 to 0.1 V (vs. RHE) for HER or

in an O_2-saturated 0.1 mol/L $HClO_4$ in the potential range 0–1.1 V (vs. RHE) for ORR, both at a scan rate of 10 mV/s.

For RRDE measurements, the ring potential was set at 1.25 V (vs. RHE). The $\%HO_2^-$ and electron transfer number (n) were determined using the followed equations:

$$\%HO_2^- = 200 \times \frac{I_r/N}{I_d + I_r/N}, \quad (1)$$

$$n = 4 \times \frac{I_d}{I_d + I_r/N}, \quad (2)$$

where I_d and I_r are the disk current and ring current, respectively, and N represents the current collection efficiency (0.44 herein).

The transfer number is calculated by the Koutecky-Levich (K-L) equation:

$$1/J = 1/J_k + 1/B\omega^2, \quad (3)$$

where $B = 0.62nFAv^{-1/6}C_0(D_0)^{2/3}$.

Zn-O_2 battery preparation. Zinc-O_2 batteries are composed of an O_2 cathode, a zinc anode and a 6.0 mol/L KOH electrolyte. The O_2 cathode includes three parts: an O_2 diffusion electrode as the catalyst, a waterproof membrane for preventing the leakage of alkali solution and foamed nickel as the current collector and skeleton of the O_2 cathode. Herein, the O_2 diffusion electrode was prepared by uniformly applying catalyst ink onto a carbon paper substrate for the gas diffusion layer, with a catalyst loading of 0.5 mg/cm^2. A polished zinc foil (0.5 mm thickness) was used as the zinc anode. Approximately 1.0 cm^2 of the electrolyte was exposed to the electrodes.

Zn-O_2 batteries test. All Zn-O_2 batteries were tested at room temperature. The polarization curve was determined via LSV (5 mV/s) using a VersaSTAT4 electrochemical working station. Both current density and power density were normalized by the exposed area of electrode. The galvanostatic discharge curve was deduced using a LAND testing system.

The specific capacity was calculated according the following equation:

$$\text{Specific capacity} = (\text{current} \times \text{service hours})/ \times (\text{weight of consumed zinc})$$

3. Results and discussion

As illustrated in Scheme 1, urea and glucose were mixed with Co^{2+}-SCN^- derived from $CoCl_2$ and NaSCN. The mixed solid was calcined at 800 °C to obtain SACo-N/C-pre. Finally, SACo-N/C was acquired by further soaking SACo-N/C-pre in 0.5 mol/L H_2SO_4 at 80 °C for 8 h. Fig. S1 (online) shows SEM images of SACo-N/C, revealing that SACo-N/C appears to be an extremely crumpled, sheet-like, two-dimensional structure. TEM and STEM images also show that SACo-N/C possesses transparent and crumpled features, regarded as the structural characteristics of thin, graphene-like carbon materials (Fig. 1a and b). Irregular fringes derived from the graphene with approximately 5 layers (1.5–2 nm) have been observed in high-resolution TEM (HRTEM) in Fig. S2 (online), further indicating that SACo-N/C is composed of a thin graphene structure. With the exception of the carbon layer, other Co-rich particles or onion-like carbon shells are absent from SACo-N/C in TEM images, suggesting that Co@C was not generated in SACo-N/C. On the contrary, Co@C features are visible in the catalyst synthesized using $CoCl_2$ as the metal precursor (Co-N/C) (Fig. S3 online), implying that SCN^- hampers Co@C formation and/or induces the elimination of Co-rich particles. To further investigate the structural details of SACo-N/C, aberration-corrected HAADF-STEM was employed to observe SACo-N/C, clearly showing single Co atoms homogeneously dispersed throughout the carbon matrix, distinguishable as brighter spots (Fig. 1c and d). These may be individual Co atoms rather than Co-rich particles existing in SACo-N/C, confirming again the importance of added SCN^- during the formation of SACo-N/C-pre, in which Co-rich particles may be completely acid etched. Furthermore, energy-dispersive X-ray spectroscopy (EDX) mapping (Fig. 1e–g) results confirm that elemental C, O, N, Co, and S are uniformly distributed in SACo-N/C. Co content is approximately 2.16 wt%, suggesting relatively high Co content in SACo-N/C. These results, combined, demonstrate that SCN^- is beneficial for the formation of a high concentration of single Co atoms.

XRD, Raman spectroscopy and XPS have also been conducted to further confirm the structural characters and detailed chemical composition of SACo-N/C (Fig. 2). As expected, there are no peaks related to the crystalline Co-rich particles but instead a broad graphitic (0 0 2) peak around 26° in the XRD pattern of SACo-N/C (Fig. 2a), while two additional sharp peaks located at 44.3° (Co (1 1 1)) and 51.6° (Co(2 0 0)) were observed in the XRD pattern of Co-N/C (Fig. S4a online). The Raman spectra of Co-N/C do not show peaks of oxides or other particles in SACo-N/C (500–900 cm^{-1}), which is similar to that of N/C fabricated without a metal precursor, suggesting again that the Co element in SACo-N/C may be in the form of atoms rather than particles (Fig. 2b and S4b (online)) [41,42]. Inevitably, the two characteristic peaks of carbon around 1350 cm^{-1} (D band, disordered carbon) and 1600 cm^{-1} (G band, graphitic carbon) are present (Fig. 2b). The higher intensity of the D band relative to the G band in SACo-N/C indicates abundant surface defects in SACo-N/C, which may enhance its catalytic activity. Additionally, a broad peak, detected simultaneously at 2500–3200 cm^{-1}, belongs to the overlay of the 2D band and D + G band, suggesting that SACo-N/C has a highly defective graphene structure, in good agreement with the results acquired from SEM and TEM [43,44]. Moreover, the XPS results demonstrate the successful doping of nitrogen and Co in the carbon matrix (Fig. 2c and d). In

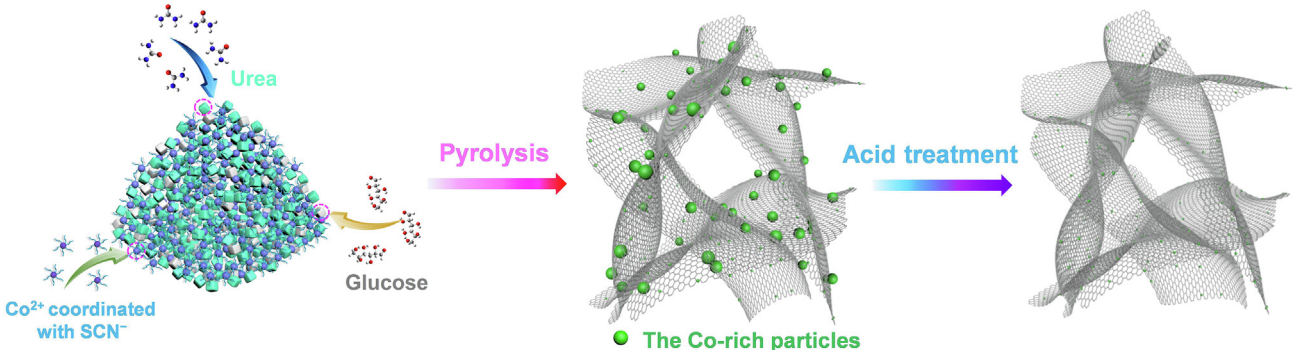

Scheme 1. (Color online) Schematic of the synthetic methods of SACo-N/C.

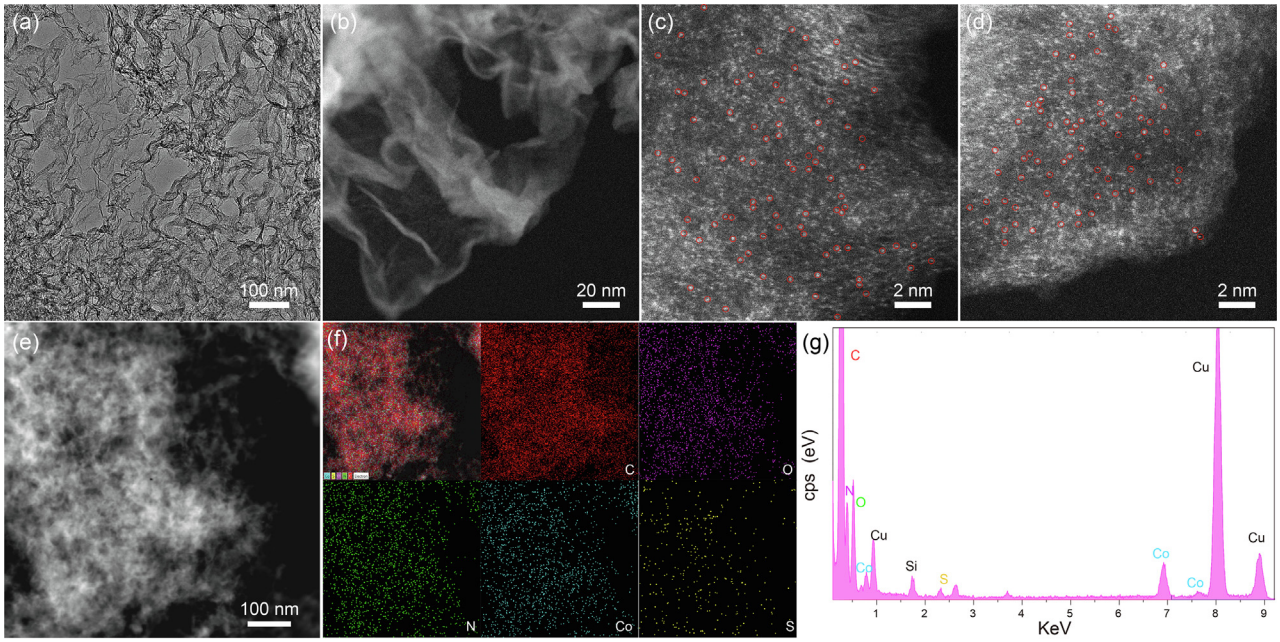

Fig. 1. (Color online) The TEM image (a), STEM image (b), HAADF-STEM images (c, d) for SACo-N/C; and several Co single atoms were circled in HAADF-STEM images. The STEM image (e) and corresponding element mapping (f) of SACo-N/C. (g) The EDX results of SACo-N/C.

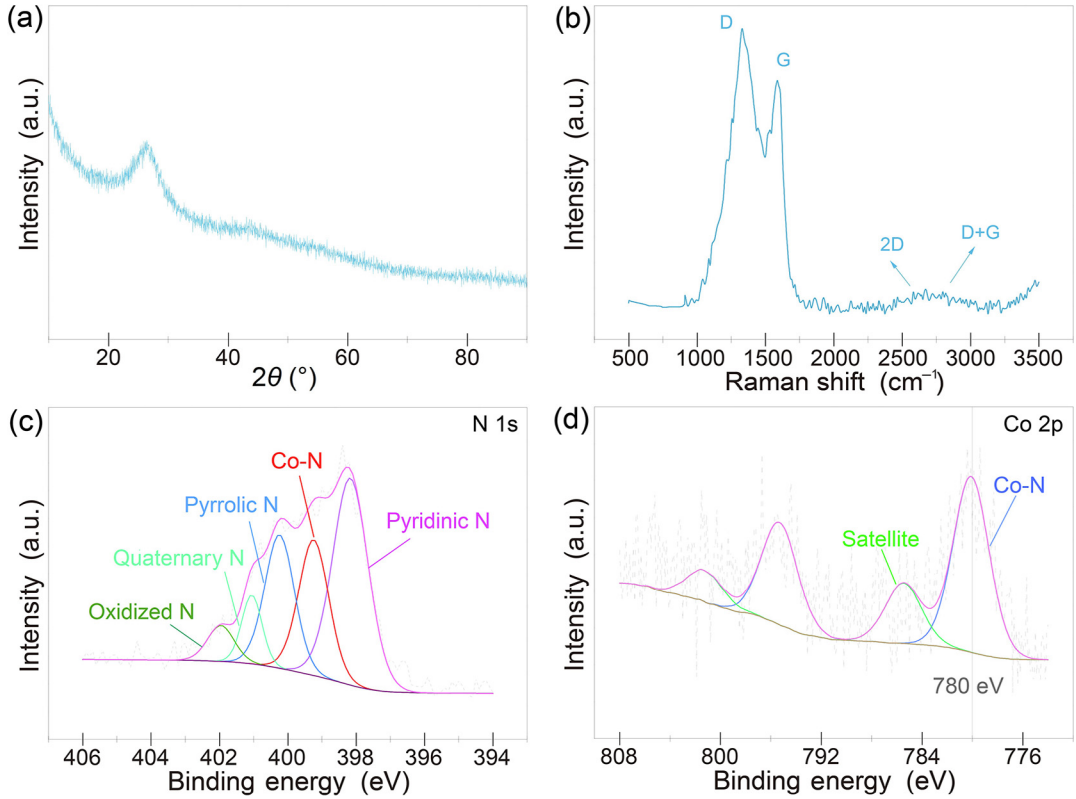

Fig. 2. (Color online) The XRD pattern (a), Raman spectrum (b), N 1s (c) and Co 2p (d) XPS spectrum of SACo-N/C.

particular, compared to the XPS spectra for Co-N/C, the peak of Co-N at 780 eV is observed in SACo-N/C rather than that of metallic Co at 778 eV, suggesting that no metallic Co particles are present in SACo-N/C (Fig. 2d and S5 (online)). The relatively high content of Co-N (2.18 at.%) in SACo-N/C can be regarded an outstanding performance.

As mentioned above, SCN^- may be the critical factor influencing the formation of structure in SACo-N/C. Inspired by the case of MOFs, the strong coordination between SCN^- and Co^{2+} was initially considered as the governing factor restricting the aggregation of Co atoms. In fact, Co-rich agglomerates have been detected in SACo-N/C-pre, thus this reason cannot explain the situation

(Fig. S6a online). However, in contrast to the broad peaks observed in the XRD pattern of Co-N/C without acid-treatment (Co-N/C-pre), sharp peaks are observed in that of SACo-N/C-pre, indicating that large but easily eliminated Co particles are present in SACo-N/C-pre. Indeed, the particle size in SACo-N/C-pre (~68.0 nm) calculated from the XRD pattern is much larger than that for Co-N/C-pre (~8.5 nm) (Fig. S6b online), indicating that the formation mechanisms of these two samples are very different. Therefore, to systematically and comprehensively investigate their mechanism of formation, we synthesized and analyzed the samples obtained at different temperatures, employing Co^{2+}-SCN^- and $CoCl_2$ as the metal precursor. Their XRD patterns are exhibited in Fig. 3a and b, respectively. It is found that crystalline compounds with Co-rich particles form at 600 °C when Co^{2+}-SCN^- is the metal precursor. In contrast, only the sample obtained at 750 °C has crystalline peaks when $CoCl_2$ is used as the metal precursor, indicating that Co-rich particles may start to form above 700 °C. To confirm this, TGA/DTA was used in a N_2 atmosphere. Fig. 3c shows that, at low temperatures (<500 °C), similar curves are present regardless of the use of TGA or DTA, related to the dehydration of precursors and the decomposition of urea. As expected, at high temperatures, the curves, especially DTA curves, differ. To observe the difference between these two curves, differential calculus has been used with respect to the DTA curves (Fig. 3d). Exothermic peaks are evident in the case where $CoCl_2$ is used as the metal precursor from 600 to 650 °C, however, no Co-rich particles have been found in the XRD pattern, indicating that the reaction occurring between 600 and 650 °C may not contribute to the formation of Co-rich particles, but is rather associated with the decomposition of atomic C_3N_4 and Co species. When temperature is increased to 750 °C, the generation of Co-rich particles and the deposition of carbon species may occur at the same time, hampering the generation of Co-rich aggregates but aiding the formation of Co@C structures, which are not in favor of the generation of Co-N_x structure due to the carbon layer obstacle (Fig. S7 online). Thus, as illustrated in Fig. 3e, after a diffusion-precipitation-agglomeration process of the coated cobalt particles, some small cobalt particles still remained in the carbon shell and some mesopores comprised by onion-like carbon shell wall may also be generated [27,45]. Thus, Co@C possess the relatively high BET surface area (427 m^2/g) and mesopore volume (Fig. S8 online). However, when Co^{2+}-SCN^- is used as the metal precursor, this compound may decompose or react in other ways. Thus, Co-rich particles form initially at 600 °C, i.e., much lower than their temperature of formation in Co-N/C. Since carbon deposition may occur around 750 °C, structural change and particle agglomeration occur without obstruction of the carbon shell together with temperature increase, resulting in the generation of large Co-rich agglomerates. The lack of BET surface area (343 m^2/g) and mesopores comprising onion-like carbon shell volumes in SACo-N/C further confirms that Co@C may not be generated in SACo-N/C (Fig. S8 online). Thus, as illustrated in Fig. 3f, it is hard for large Co-rich particles to be encapsulated completely by carbon layer to form well -encapsulated Co@C structure; thereby SACo-N/C catalysts can be generated by a "top-down" process, in which the cobalt atoms escape from Co-rich particles across discontinuous carbon layers and move to the carbon matrix and eventually are coordinated with nitrogen atoms. Moreover, the temperature of SACo-N/C generation is another important factor. As shown in Fig. S9a (online), the XRD patterns of the samples synthesized at 900 and 1,000 °C for 1 h before acid treatment (labeled

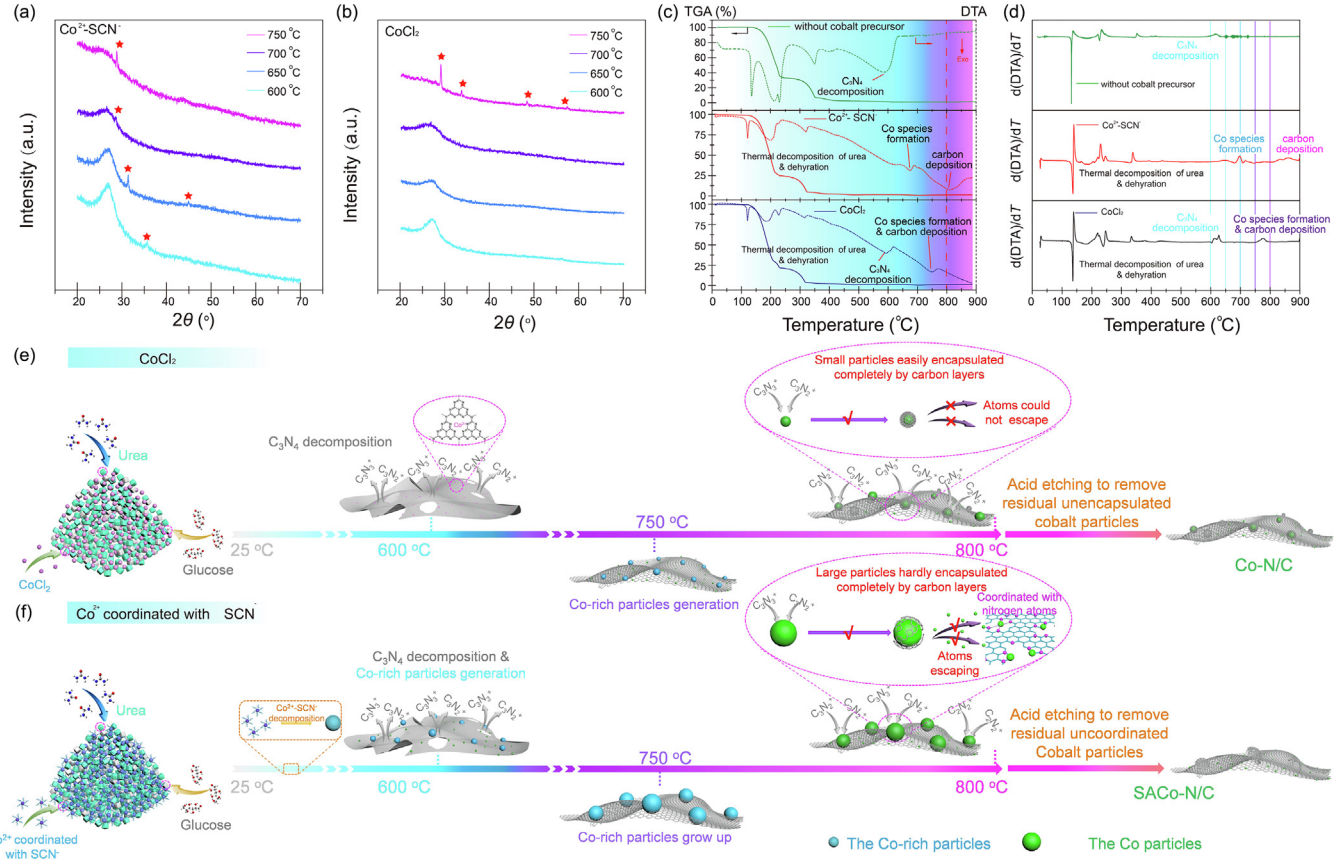

Fig. 3. (Color online) The XRD pattern of the catalysts obtained by using Co^{2+}-SCN^- (a) and $CoCl_2$ (b) as the metal precursor at different temperature, respectively (the stars represent the peak of crystalline Co-rich particles). (c) The TGA and DTA curves of the mixed precursors with Co^{2+}-SCN^- or $CoCl_2$ and without cobalt precursor; (d) the corresponding first order differential curve of DTA. The catalysts formation mechanism by using $CoCl_2$ (e) and Co^{2+}-SCN^- (f).

SACo-N/C-900-pre and SACo-N/C-1000-pre, respectively) also exhibit large agglomerates. With a temperature increase from 800 to 1,000 °C, the refinement of Co agglomerates is observed, and particle sizes decrease from ~68.0 to ~43.6 nm (Fig. S9b online). And after acid treatment, Co particles with smaller sizes remain in the SACo-N/C-900 and SACo-N/C-1000, suggesting the present of Co@C structures in these two samples (Fig. S10a online). Thus, when temperature is increased, Co agglomerates may be divided into smaller isolates separated by the carbon shell, due to the eased diffusion of carbon atoms into Co agglomerates at higher temperatures. In brief, carbon atoms would not only diffuse into Co agglomerates to successfully break large agglomerates but also coat the separated Co particles *in situ* to form Co@C at a higher temperature calcination. This further indicates that Co@C generation requires a high level of energy that cannot not be provided at 800 °C. Furthermore, the decease of ORR and HER activity is also observed in Fig. S10 (online), implying that single Co atoms are more active than coated Co particles. 800 °C is thus the proper temperature to inhibit the formation of Co@C and maintain an abundance of highly active Co atoms in the catalyst.

To further verify the catalytic activity of SACo-N/C for ORR and HER, CV were acquired. Fig. S11a (online) shows that, compared to Co-N/C and N/C, SACo-N/C exhibits the largest double-layer capacity, suggesting that is has the largest accessible areas. Linear scan voltammogram (LSV) curves in Fig. 4 demonstrate that SACo-N/C also possesses the highest activity among these three catalysts for both ORR and HER in alkaline solution. As shown in Fig. 4a, SACo-N/C reaches the highest activity with a half-wave potential

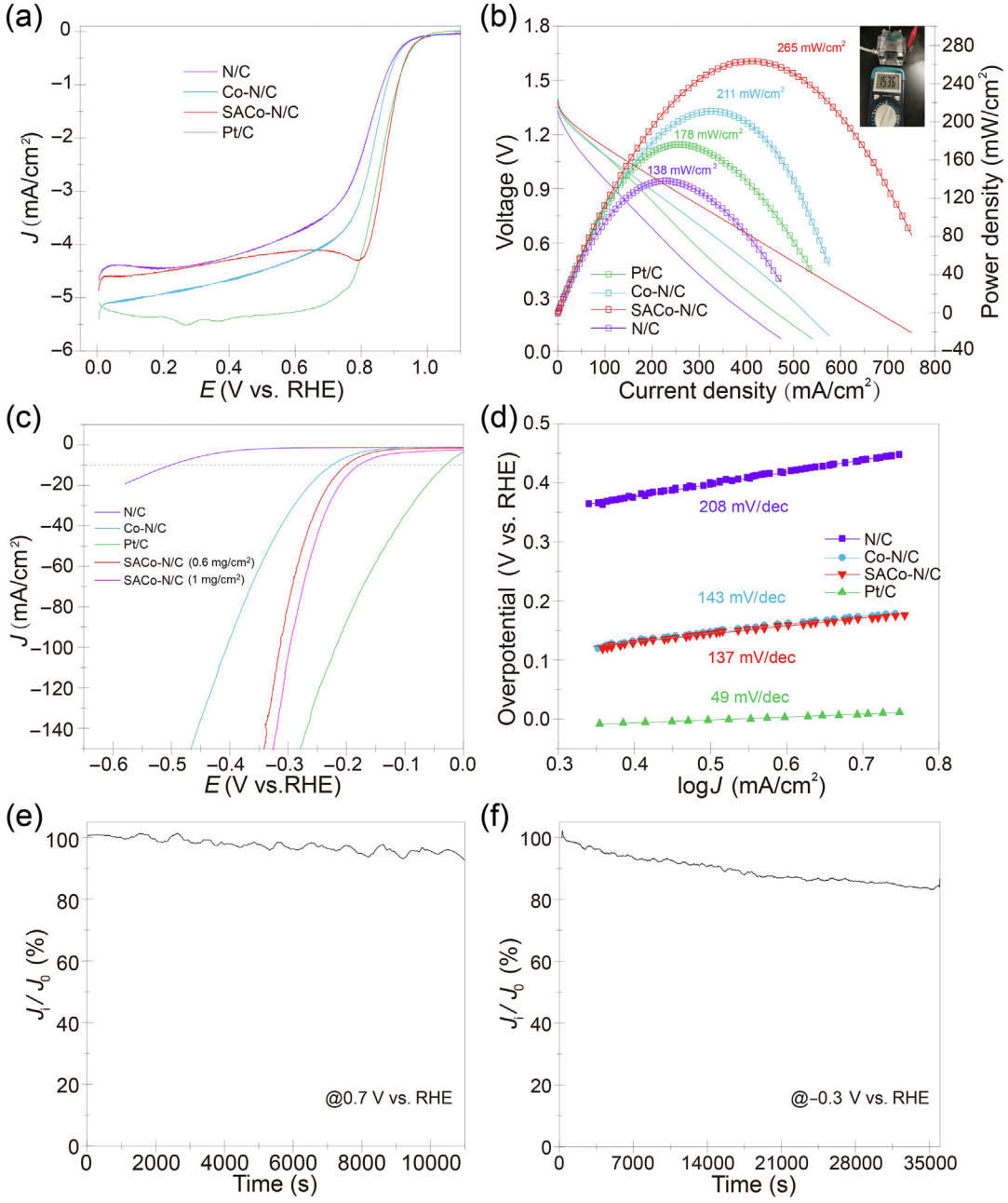

Fig. 4. (Color online) (a) The ORR LSVs for SACo-N/C, Co-N/C, N/C and 40 wt% Pt/C. (b) Discharging polarization and the corresponding power density curves of Zn-O_2 batteries using Pt/C and SACo-N/C as ORR catalyst. (c) The HER LSVs for SACo-N/C (0.6 and 1 mg/cm^2), Co-N/C, N/C and 40 wt% Pt/C, and (d) the corresponding Tafel plots. ADT test of SACo-N/C for ORR (e) and HER (f).

at 0.878 V (vs. RHE) which is more positive than that of Pt/C catalysts (0.855 V vs. RHE) and other non-precious metal catalysts (Table S1 online). The number of transferred electrons for SACo-N/C is about 3.5, indicating that SACo-N/C may follow with a 2×2 electron transfer pathway [46] (Fig. 4b and S11b, c (online)). Negligible methanol-crossover effect has been observed in Fig. S11d (online). We then constructed a Zn-O_2 battery using SACo-N/C as the O_2 electrode in a 6.0 mol/L KOH solution. This battery, with high open-circuit voltage (1.536 V), possesses its highest peak power density (266 mW/cm^2) and largest gravimetric energy density (755 mA h/g_{Zn}) at current densities of 100 mA/cm^2, which are 1.9 and 1.3 times those of Pt/C catalysts, respectively (Fig. 4b and S12 (online)). Fig. 4c shows that SCN^- and metal precursor additions result in significant improvement of HER in the case of SACo-N/C. The overpotential at a current density of 10 mA/cm^2 is found at 0.198 V for SACo-N/C, 0.219 V for Co-N/C and 0.5000 V for N/C, respectively. It is noteworthy that, when the loading of SACo-N/C increases to 1 mg/cm^2 with the increase of electrode thickness, its overpotential at a current density of 10 mA/cm^2 decreases to 178 mV, indicating that HER activity with SACo-N/C is comparable to that of state-of-the-art non-precious-metal carbon-based HER catalysts (Table S2 online). Unlike the HER mechanism of Pt/C catalysts, SACo-N/C, with the smallest Tafel slope (137 mV/decade) among the three carbon-based catalysts, possesses a Volmer-Heyrovsky reaction pathway operating with water adsorption or dissociation (i.e., a Volmer step with the theoretical value of 120 mV/decade) as the rate-limiting step, implying its positive effect on the efficiency of the HER process (Fig. 4d). ORR and HER activities of SACo-N/C were investigated in both alkaline and acid solutions. The ORR and HER activities of SACo-N/C are highest among all the three carbon-based catalysts in both (Fig. S13 online). Indeed, SACo-N/C exhibits a half-wave potential of 0.728 V (vs. RHE), which is only 73 mV negative than that of the Pt/C catalyst. Only 169 mV overpotential occurs when the HER current density reaches 10 mA/cm^2 in 0.5 mol/L H_2SO_4. Overall, the SACo-N/C shows superior ORR and HER activity, which may be closely associated with its single Co atom-doped graphene structure. Since the presence of surface defects and degree of graphitic nature of SACo-N/C and Co-N/C is similar, the absence of Co nanoparticles and the higher surface Co content (0.64 at.%) of SACo-N/C when compared to that of Co-N/C (0.47 at.%) can be regarded as the dominant reason for the superior performance of SACo-N/C in ORR and HER. Furthermore, the durability of SACo-N/C in ORR and HER were also measured, as shown in Fig. 4e, f. After 11,000 s continuous catalysis, negligible degradation in activity was observed in ORR, reflecting an excellent durability. The durability of SACo-N/C in HER is also good, with approximately 85% current retention after 10 h continuously working at −0.3 V (vs. RHE). After a HER accelerated degradation test, there were still no agglomerated particles in SACo-N/C, indicative of its superb structure stability (Fig. S14 online). Furthermore, the discharge voltage decreases only by 7% (from 1.30 to 1.21 V) after 80 h discharging, indicating that SACo-N/C is good in stability in operation of Zn-O_2 battery. Overall, we find that SACo-N/C may be a promising alternative for Pt/C catalysts in fuel cells, water-splitting devices and Zn-O_2 batteries.

4. Conclusion

In summary, we have reported a straightforward and cost-effective strategy for the fabrication of a SACo-N/C graphene catalyst in the presence of Co^{2+}-SCN^-. Co^{2+}-SCN^- plays an important role in the generation of SACo-N/C by separating the temperatures for the generation of Co-rich particles and deposition of carbon. We demonstrate that this separated temperature effectively inhibits the formation of Co@C structures and thus provides the possibility for the cobalt atoms escaping from Co-rich particles across discontinuous carbon layers and moving to the carbon matrix and eventually being coordinated with nitrogen atoms to form SACo-N/C catalysts. Hence, our findings offer a novel strategy for the fabrication of high-performance single atom M-N/C catalysts through using some ligands to coordinate the metal ion and thereby control the temperature difference between the generation of metal-rich particles and the deposition of carbon.

Conflict of interest

The authors declare that they have no conflict of interest.

Acknowledgments

This work was supported by the National Key Research and Development Program of China (2016YFB0101202), the National Natural Science Foundation of China (21761162015, 91534205, 21436003) and the Fundamental Research Funds for the Central Universities.

Author contributions

Yao Wang and Linhui Chen designed and accomplished the experiments together. All authors discussed the results. Zidong Wei, Zhanxin Mao, Lishan Peng, Rui Xiang, Jianghai Deng, Xianyi Tang and Qiang Liao co-wrote the paper.

Appendix A. Supplementary data

Supplementary data to this article can be found online at https://doi.org/10.1016/j.scib.2019.06.012.

References

[1] Xiang R, Tong C, Wang Y, et al. Hierarchical coral-like FeNi(OH)$_x$/Ni via mild corrosion of nickel as an integrated electrode for efficient overall water splitting. Chin J Catal 2018;39:1736–45.
[2] Xu P, Zhang J, Jiang G, et al. Embellished hollow spherical catalyst boosting activity and durability for oxygen reduction reaction. Nano Energy 2018;51:745–53.
[3] Zhang J, Chen G, Müllen K, et al. Carbon-rich nanomaterials: fascinating hydrogen and oxygen electrocatalysts. Adv Mater 2018;30:1800528.
[4] Wang Y, Li J, Wei Z. Transition-metal-oxide-based catalysts for the oxygen reduction reaction. J Mater Chem A 2018;6:8194–209.
[5] Wang S, Jang H, Wang J, et al. Cobalt-tannin-framework-derived amorphous Co-P/Co-N-C on N, P Co-doped porous carbon with abundant active moieties for efficient oxygen reactions and water splitting. ChemSusChem 2019;12:830–8.
[6] Bai X, Ling C, Shi L, et al. Insight into the catalytic activity of MXenes for hydrogen evolution reaction. Sci Bull 2018;63:1397–403.
[7] Yan J, Chen L, Liang X. Co_9S_8 nanowires@NiCo LDH nanosheets arrays on nickel foams towards efficient overall water splitting. Sci Bull 2019;64:158–65.
[8] Peng L, Shah SSA, Wei Z. Recent developments in metal phosphide and sulfide electrocatalysts for oxygen evolution reaction. Chin J Catal 2018;39:1575–93.
[9] Wang Y, Li J, Wei Z. Recent progress of carbon-based materials in oxygen reduction reaction catalysis. ChemElectroChem 2018;5:1764–74.
[10] Wu Z, Wang J, Song M, et al. Boosting oxygen reduction catalysis with N-doped carbon coated Co_9S_8 microtubes. ACS Appl Mater Interfaces 2018;10:25415–21.
[11] Song M, Zhang Z, Li Q, et al. Ni-foam supported Co(OH)F and Co-P nanoarrays for energy-efficient hydrogen production via urea electrolysis. J Mater Chem A 2019;7:3697–703.
[12] Zhong L, Jensen JO, Cleemann LN, et al. Electrochemical probing into the active sites of graphitic-layer encapsulated iron oxygen reduction reaction electrocatalysts. Sci Bull 2018;63:24–30.
[13] Wu Z, Wang J, Liu R, et al. Facile preparation of carbon sphere supported molybdenum compounds (P, C and S) as hydrogen evolution electrocatalysts in acid and alkaline electrolytes. Nano Energy 2017;32:511–9.
[14] Wu Z, Song M, Wang J, et al. Supramolecular gel assisted synthesis of Co_2P nanosheets as an efficient and stable catalyst for oxygen reduction reaction. New J Chem 2018;42:8800–4.

[15] Wu Z, Nie D, Song M, et al. Facile synthesis of Co-Fe-BP nanochains as efficient bifunctional electrocatalysts for overall water-splitting. Nanoscale 2019;11:7506–12.
[16] Gao X, Li X, Kong Z, et al. Bifunctional 3D n-doped porous carbon materials derived from paper towel for oxygen reduction reaction and supercapacitor. Sci Bull 2018;63:621–8.
[17] Seh ZW, Kibsgaard J, Dickens CF, et al. Combining theory and experiment in electrocatalysis: insights into materials design. Science 2017;355:eaad4998.
[18] Wang J, Wei ZD. Recent progress in non-precious metal catalysts for oxygen reduction reaction. Acta Phys Chim Sin 2017;33:886–902.
[19] Wang J, Xu F, Jin H, et al. Non-noble metal-based carbon composites in hydrogen evolution reaction: fundamentals to applications. Adv Mater 2017;29:1605838.
[20] Yang XD, Chen C, Zhou ZY, et al. Advances in Active site structure of carbon-based non-precious metal catalysts for oxygen reduction reaction. Acta Phys Chim Sin 2018;35:472–85.
[21] Meng FL, Wang ZL, Zhong HX, et al. Reactive multifunctional template-induced preparation of Fe-N-doped mesoporous carbon microspheres towards highly efficient electrocatalysts for oxygen reduction. Adv Mater 2016;28:7948–55.
[22] Wu G, More KL, Johnston CM, et al. High-performance electrocatalysts for oxygen reduction derived from polyaniline, iron, and cobalt. Science 2011;332:443–7.
[23] Peng H, Hou S, Dang D, et al. Ultra-high-performance doped carbon catalyst derived from *o*-phenylenediamine and the probable roles of Fe and melamine. Appl Catal B Environ 2014;158:60–9.
[24] Wang Y, Nie Y, Ding W, et al. Unification of catalytic oxygen reduction and hydrogen evolution reactions: highly dispersive Co nanoparticles encapsulated inside Co and nitrogen co-doped carbon. Chem Commun 2015;51:8942–5.
[25] Xiao M, Zhu J, Feng L, et al. Meso/macroporous nitrogen-doped carbon architectures with iron carbide encapsulated in graphitic layers as an efficient and robust catalyst for the oxygen reduction reaction in both acidic and alkaline solutions. Adv Mater 2015;27:2521–7.
[26] Kim JH, Sa YJ, Jeong HY, et al. Roles of Fe-N_x and Fe-Fe_3C@ C species in Fe-N/C electrocatalysts for oxygen reduction reaction. ACS Appl Mater Interfaces 2017;9:9567–75.
[27] Wang Y, Chen W, Chen Y, et al. Carbon-based catalysts by structural manipulation with iron for oxygen reduction reaction. J Mater Chem A 2018;6:8405–12.
[28] Wang JY, Ouyang T, Li N, et al. S, N co-doped carbon nanotube-encapsulated core-shelled CoS_2@Co nanoparticles: efficient and stable bifunctional catalysts for overall water splitting. Sci Bull 2018;63:1130–40.
[29] Zhu C, Fu S, Shi Q, et al. Single-atom electrocatalysts. Angew Chem Int Ed 2017;56:13944–60.
[30] Chen Y, Ji S, Chen C, et al. Single-atom catalysts: synthetic strategies and electrochemical applications. Joule 2018;2:1242–64.
[31] Wang J, Huang Z, Liu W, et al. Design of N-coordinated dual-metal sites: a stable and active Pt-free catalyst for acidic oxygen reduction reaction. J Am Chem Soc 2017;139:17281–4.
[32] Zhu QL, Xia W, Zheng LR, et al. Atomically dispersed Fe/N-doped hierarchical carbon architectures derived from a metal–organic framework composite for extremely efficient electrocatalysis. ACS Energy Lett 2017;2:504–11.
[33] Fu S, Zhu C, Su D, et al. Porous carbon-hosted atomically dispersed iron-nitrogen moiety as enhanced electrocatalysts for oxygen reduction reaction in a wide range of pH. Small 2018;14:1703118.
[34] Yi JD, Xu R, Wu Q, et al. Atomically dispersed iron-nitrogen active sites within porphyrinic triazine-based frameworks for oxygen reduction reaction in both alkaline and acidic media. ACS Energy Lett 2018;3(4):883–9.
[35] Wei W, Shi X, Gao P, et al. Well-elaborated, mechanochemically synthesized Fe-TPP⊂ZIF precursors (Fe-TPP=tetraphenylporphine iron) to atomically dispersed iron-nitrogen species for oxygen reduction reaction and Zn-air batteries. Nano Energy 2018;52:29–37.
[36] Chen W, Pei J, He CT, et al. Rational design of single molybdenum atoms anchored on N-doped carbon for effective hydrogen evolution reaction. Angew Chem Int Ed 2017;56:16086–90.
[37] Han Y, Wang YG, Chen W, et al. Hollow N-doped carbon spheres with isolated cobalt single atomic sites: superior electrocatalysts for oxygen reduction. J Am Chem Soc 2017;139:17269–72.
[38] Li S, Cheng C, Zhao X, et al. Active salt/silica-templated 2D mesoporous FeCo-N_x-carbon as bifunctional oxygen electrodes for zinc-air batteries. Angew Chem Int Ed 2018;57:1856–62.
[39] Zhang H, Hwang S, Wang M, et al. Single atomic iron catalysts for oxygen reduction in acidic media: particle size control and thermal activation. J Am Chem Soc 2017;139:14143–9.
[40] Cheng C, Li S, Xia Y, et al. Atomic Fe-N_x coupled open-mesoporous carbon nanofibers for efficient and bioadaptable oxygen electrode in Mg-Air batteries. Adv Mater 2018;30:1802669.
[41] Hadjiev VG, Iliev MN, Vergilov IV. The raman spectra of Co_3O_4. J Phys C Solid State Phys 1988;21:L199.
[42] Tang CW, Wang CB, Chien SH. Characterization of cobalt oxides studied by FT-IR, Raman, TPR and TG-MS. Thermochim Acta 2008;473:68–73.
[43] Tao L, Qiu C, Yu F, et al. Modification on single-layer graphene induced by low-energy electron-beam irradiation. J Phys Chem C 2013;117:10079–85.
[44] Pimenta MA, Dresselhaus G, Dresselhaus MS, et al. Studying disorder in graphite-based systems by Raman spectroscopy. Phys Chem Chem Phys 2007;9:1276–90.
[45] Wu G, Nelson M, Ma S, et al. Synthesis of nitrogen-doped onion-like carbon and its use in carbon-based CoFe binary non-precious-metal catalysts for oxygen-reduction. Carbon 2011;49:3972–82.
[46] Olson TS, Pylypenko S, Atanassov P, et al. Anion-exchange membrane fuel cells: dual-site mechanism of oxygen reduction reaction in alkaline media on cobalt- polypyrrole electrocatalysts. J Phys Chem C 2010;114:5049–59.

Yao Wang received his B.E. and Ph.D. degrees from Chongqing University in 2013 and 2018, respectively. Now he is a distinguished associate research fellow in Sichuan University. His current research interests focus on the development of novel materials for electrochemical catalyst.

Linhui Chen received her B.E. degree from Xinyang Normal University in 2016. Now she is a Master student at Chongqing University. Her current research interests focus on the development of carbon-based materials for fuel cell and water-splitting devices.

Zidong Wei received his Ph.D. degree from Tianjin University in 1994. Currently, he is Full Professor at Chongqing University. His research interests include electrocatalysis, computational studies, electrochemical materials and their applications in catalysis and energy storage.